

SIMULATIONS OF RADIATION DRIVEN OUTFLOWS IN SUPER-EDDINGTON ATMOSPHERES

CHRISTOPHER C. LINDNER, MILOŠ MILOSAVLJEVIĆ,

Department of Astronomy, University of Texas, 1 University Station C1400, Austin, TX 78712

Draft version May 16, 2014

ABSTRACT

Winds driven by super-Eddington outflows, where the outward force of radiation exceeds the inward force of gravity, are present in a multitude of astrophysically relevant systems, such as mass loss from massive stars, supercritical flows onto black holes, supermassive stars, and classical novae. Observational and theoretical studies have suggested that in at least some cases, these winds cannot be homogeneous, and layers of the flow will be subject to a variety of instabilities. The exact nature of these instabilities is difficult to determine analytically, and, until recently, multidimensional simulations of these systems have been beyond our computational limitations.

Here we present the results of multidimensional radiation hydrodynamics (RHD) simulations of super-Eddington atmospheres using a modified version of the RHD solver in the FLASH code. We simulate an initially sub-Eddington flux entering the base of very optically thick atmospheres and observe the transition from a radiatively inefficient, convective layers to the outer clumpy layers, and finally to the supersonic outflow layers as the flux becomes super-Eddington. We also present our verification testing for our modifications of the FLASH code, to make it suitable for astrophysical RHD problems.

Subject headings: stars: winds, outflows — supernovae: general

1. INTRODUCTION

In situations where the outward force of radiation leaving a system exceeds the inward gravitational pull of the system, radiative feedback can drive an outflow. These "super-Eddington" (SE) winds are relevant in many astrophysical systems, including winds and outbursts from massive stars (e.g. η Car), the atmospheres of supermassive stars (see, e.g., Dotan & Shaviv 2012) rapidly accreting black holes, classical novae, and protostellar feedback. Although a large body of theoretical research exists on such flows, few multidimensional RHD simulations of SE atmospheres are present in the literature. The nature of the clumpiness, turbulence, and transition from a radiatively inefficient flow to a potentially supersonic, radiatively-driven outflow are still relatively unknown, and are the focus of this work.

Theoretical modeling of the observations of the SE outburst of η Car have shown that its high velocity, relatively low mass outflows cannot be described a steady state, homogeneous outflow; Shaviv (2000) found that if the structure of the outflows of η Car were homogeneous, then the transition from a convective or advective region to a radiation dominated region would occur deep in the atmosphere (optical depth, $\tau > 300$). At this depth, the mass of the atmosphere far exceeds the mass of the observed outflows, and the relative Eddington factor (the ratio of specific outward radiation force and the specific gravitational force) would likely be below unity. As a result, material would have difficulty reaching the escape velocity, and any outflows would be expected to be less luminous, slower moving, and more massive than those we actually observe. Shaviv (2000) find that the atmosphere of η Car must be porous, allowing more radiation to escape from deep in the atmosphere, and lowering the mass of the outflow region. Similar analysis has been applied to novae as well (Shaviv 2001).

In further support of this notion, there is evidence for many different RHD instabilities to arise in sub-Eddington and SE atmospheres, including the radiative Rayleigh-Taylor instabil-

ity (Krumholz et al. 2009; Jacquet & Krumholz 2011), "photon bubbles" (Blaes & Socrates 2003), and the formation of stationary and moving wave patterns (see, e.g., Spiegel & Tao 1999; Shaviv 2000, 2001, and references therein). Each of these instabilities can result in an overall "clumpiness" to the flow, which will decrease the effective optical depth in the critical region. However, it is important to note that it is difficult to predict which of these processes will dominate in such an atmosphere, as few multidimensional simulations have been done of such systems.

This line of reasoning gives us a simple schematic of the structure of a radiation source deeply embedded in a highly optically thick atmosphere, which can then drive supersonic winds in its photosphere. Deep in the atmosphere, energy transport via radiative diffusion is inefficient, and energy transport is dominated by convection. Higher in the atmosphere, radiative diffusion will dominate the luminosity of the atmosphere. For many astrophysically relevant atmospheres, this critical transition point would be located at a very high optical depth in the star. However, to drive a fast-moving outflow, this region must lower its effective optical depth, possibly via inhomogeneous RHD instabilities. This enables the transfer of much radiation flux, with little transfer of force. Higher in the atmosphere, these perturbations will lower in density and become transparent. From this region and up through the photosphere, the flow is SE, and potentially, a supersonic outflow will be driven.

van Marle et al. (2009) performed one dimensional hydrodynamic simulations of SE stellar winds with a parameterized radiative momentum injection prescription. Because these models were one dimensional, the precise nature of the necessary fluid instabilities were not reproduced ab initio, but instead a clumpy layer was assumed, parameterized, and put in by hand. They found that a number of rising and falling shells formed in the wind structure, and at large radii an outflow was driven, and indicated multidimensional RHD simulations are necessary to fully understand the complex radiation-matter interactions in this system.

Krumholz & Thompson (2012), and later, Krumholz & Thompson (2013) performed the first multidimensional, RHD simulations of radiative atmospheres resembling the conditions of protostellar feedback in a young star cluster. They found that optically thick material in the winds was subject to the radiative Rayleigh-Taylor instability, and gas confined itself into thin filaments, decreasing the effective optical depth of the gas and limiting the momentum transfer from the radiation to the gas. However, the atmospheres they investigated had relatively low optical depths ($\tau < 10$), and did not include the deep, convective atmosphere or the transitional instability region.

The focus of this project is to expand on the limited body of RHD simulations of SE atmospheres by simulating a radiation source embedded in a high optical depth, gravitationally bound atmosphere, which will drive supersonic winds at large radii. We investigate the formation of instabilities in the boundary layers, and the properties of the outflows in such a system. In Section 2 we discuss the RHD solver used and the modifications required for the project, in Section 3 we discuss our verification tests of this new code, in Section 4 we discuss the parameters chosen for our model and our simulation setup, in Section 5 we present the results of our simulation, in Section 6 we discuss the implications of our results, and in Section 7 we summarize.

2. NUMERICAL ALGORITHM

Our simulations were carried out with the piecewise parabolic method (PPM) solver in the adaptive-mesh refinement code FLASH (Fryxell et al. 2000), version 4.0, in two spatial dimensions. FLASH has recently implemented a RHD solver supporting multi-group flux-limited diffusion (FLD) utilizing a fully implicit diffusion solver and an explicit solver for matter-radiation coupling, and can track a full three temperature (3T), three component fluid made of free electrons, ions, and radiation. For our purposes, portions of the solver needed to be modified, especially the radiation-matter coupling solver. In Section 2.1, we describe the three species hydrodynamics solver in FLASH. In Section 2.2, we describe the diffusion solver. In Section 2.3, we describe the radiation-matter coupling solver, and our modifications to it.

2.1. FLASH Multispecies Hydrodynamics

The basic equations of hydrodynamics solved by the FLASH multispecies solver are mass conservation

$$\partial_t \rho + \nabla \cdot (\rho \mathbf{v}) = 0, \quad (1)$$

momentum conservation

$$\partial_t (\rho \mathbf{v}) + \nabla \cdot (\rho \mathbf{v} \mathbf{v}) + \nabla P_{\text{tot}} = 0, \quad (2)$$

total energy conservation,

$$\partial_t (\rho E_{\text{tot}}) + \nabla \cdot [(\rho E_{\text{tot}} + P_{\text{tot}}) \mathbf{v}] = 0, \quad (3)$$

and the individual equations for internal energy advection. In the three temperature, radiation hydrodynamics unit of FLASH, energy advection is split into three equations, one for each species

$$\partial_t (\rho \epsilon_{\text{ele}}) + \nabla \cdot [\rho \epsilon_{\text{ele}} \mathbf{v}] = 0, \quad (4)$$

$$\partial_t (\rho \epsilon_{\text{ion}}) + \nabla \cdot [\rho \epsilon_{\text{ion}} \mathbf{v}] = 0, \quad (5)$$

$$\partial_t (\rho \epsilon_{\text{rad}}) + \nabla \cdot [\rho \epsilon_{\text{rad}} \mathbf{v}] = 0. \quad (6)$$

FLASH then calculates the changes in total energy due to hydrodynamic work and shock heating and distributes this energy among the species according to the ratios of pressures in a "RAGE-like" approach (Gittings et al. 2008). This is carried out in four steps:

1. Equations 1, 2, 3, 4, 5, and 6 are evolved simultaneously and internal energies are updated to reflect changes due to advection.
2. The change in total specific internal energy is calculated via $\Delta \epsilon_{\text{tot}} = \Delta E_{\text{tot}} - \mathbf{v} \cdot \mathbf{v} / 2$.
3. The change in specific internal energy due to hydrodynamic work and shock heating is calculated via $\Delta \epsilon_{\text{tot}}^{\text{work}} + \Delta \epsilon_{\text{tot}}^{\text{shock}} = \Delta \epsilon_{\text{tot}} - \Delta \epsilon_{\text{tot}}^{\text{adv}}$, where $\Delta \epsilon_{\text{tot}}^{\text{adv}}$ is the change in specific internal energy solely due to advection.
4. The energy $\Delta \epsilon_{\text{tot}}^{\text{work}} + \Delta \epsilon_{\text{tot}}^{\text{shock}}$ is distributed evenly among all three species according to the ratio of their pressures.

This method ensures that energy is distributed among the species correctly in smooth flows, but may fail to do so near shocks¹. By advecting each species separately, we are able to maintain separate temperatures for the gas and radiation. The equations above do not account for energy gains or losses from radiative diffusion, radiation-matter coupling, gravity, or artificial heating source terms. These components are carried out operator-split from the equations above.

2.2. Radiative Diffusion

FLASH version 4.0 is capable of multigroup FLD, within certain limitations. Here, we reproduce the basic multigroup diffusion equations from the FLASH User Guide and from manual inspection of the code and indicate where we have modified the code accordingly. The multigroup FLD solver in FLASH supports inhomogeneous, non-blackbody distributions of photons by dividing the radiation field into a user-defined number of energy ranges or "groups." This enables the user to diverge from the "gray atmosphere" approximation used in standard FLD approaches. The multigroup radiative diffusion equation is

$$\frac{1}{c} \partial_t u_{\text{rad},g} - \nabla \cdot (D_g \nabla u_{\text{rad},g}) = 0, \quad (7)$$

where c is the speed of light, g is the group index, u_{rad} is the energy density of radiation,

$$D_g = \frac{c}{3\sigma_{t,g} + \frac{|\nabla u_{r,g}|}{\alpha_r u_{r,g}}}, \quad (8)$$

such that $D_g \approx \frac{c}{3\sigma_{t,g}}$ for optically thick regions and $D_g \approx \frac{\alpha_{\text{rad}} c u_{r,g}}{|\nabla u_{r,g}|}$ such that $\nabla \cdot D_g \nabla u_{r,g} = \nabla \alpha_{\text{rad}} c u_g$ for optically thin regions (α_{rad} is a dimensionless coefficient, set to unity in our simulations), σ_t is transport opacity, and c is the speed of light. For our purposes, we choose not to take advantage of the multigroup functionality, and only consider a single energy band, and therefore drop the group indices in our implementation.

¹ For further justification and explanation of radiation hydrodynamics unit in FLASH, consult the FLASH Users Guide version 4 available at <http://flash.uchicago.edu/>.

FLASH solves Equation 7 using a fully implicit diffusion solver. The `hypre` parallel linear equation solver library is used to efficiently perform the diffusion calculations. Because the solver is implicit, it is not subject to any timestep constraint for stability. The solver requires its own set of boundary conditions outside of the hydrodynamic ones. We describe our boundary conditions in Section 4. Outside of our simplification of using only a single wavelength band (reverting the code back to a "gray atmosphere"), we do not impose any other changes to the implicit diffusion solver.

2.3. Unmodified FLASH Radiation-Matter Coupling

The FLASH RHD solver handles the transfer of energy to and from electrons and the radiation field via

$$\frac{1}{c} \partial_t u_{\text{rad},g} + \sigma_{a,g} u_{\text{rad},g} = \sigma_{e,g} a T_{\text{ele}}^4 \frac{15}{\pi^4} \left[\int_{x_g}^{x_{g+1}} dx' \frac{x'^3}{e^{x'} - 1} \right], \quad (9)$$

where σ_a is absorption opacity, and σ_e is emission opacity (related to emissivity), and $x \equiv \frac{h\nu}{k_B T_e}$, where ν is frequency, h is Planck's constant, k_B is Boltzmann constant, $a = \frac{4\sigma_{SB}}{c}$ is the radiation constant, and σ_{SB} is the Stephan-Boltzmann constant. In the single group, gray atmosphere approximation, Equation 9 simplifies to

$$\frac{1}{c} \partial_t u_{\text{rad}} + \sigma_a u_{\text{rad}} = \sigma_e a T_{\text{ele}}^4. \quad (10)$$

The time derivative of u_{ele} due to absorption or emission of energy from the radiation field is

$$\partial_t u_{\text{ele}} = -\partial_t u_{\text{rad}}. \quad (11)$$

The standard RHD solver in FLASH will not transfer energy between the electrons and ions. Instead, this is handled by a separate material conduction unit in FLASH, making FLASH a true, three temperature (3T) RHD solver. However, for most astrophysical applications, any relevant dynamical timescales are likely many orders of magnitude greater than any heat conduction timescales. Our modifications to account for this issue are described in Section 2.4.

In the standard FLASH RHD solver, equation 9 is solved via finite differencing, and is operator split from the diffusion calculations described in 2.2. Morel & McClarren (2011) find that the maximum stable timestep due to radiative absorption using the finite differencing used by FLASH is given by

$$\Delta t_{\text{max,rad}} = \alpha_r \left| \frac{2c_{V,e}}{\sigma_a c \left(\frac{\partial B}{\partial T_e} - c_{V,e} \right)} \right|, \quad (12)$$

where α_r is a parameter set to unity, $c_{V,e}$ is the specific heat capacity of the electrons at constant volume and $\frac{\partial B}{\partial T} = 4aT_e^3$ if only one radiation group is used. The electron specific heat capacity at constant volume, $c_{V,e}$, is given by

$$c_{V,e} = \frac{RZ}{\bar{A}(\gamma-1)}, \quad (13)$$

where R is the gas constant, Z is the atomic number, \bar{A} is the mean atomic mass, and the γ is the adiabatic index for the electrons. Because radiation diffusion is carried out implicitly, no additional timestep constraint is required for the radiation unit.

For gases where the optical depth is relatively high, this condition becomes unmanageably restrictive when compared

to the Courant condition. As a result, this timestep limitation is included in FLASH, but disabled by default. However, in our testing for astrophysical applications, the code has proven to be unstable without this timestep limitation in place. We expect regions of high opacity in our simulations, therefore we cannot use this restriction as-is. One potential solution to this issue is to use a single-temperature method where at all times $T_{\text{ion}} = T_{\text{ele}} = T_{\text{rad}}$. This assumption is valid in the static diffusion limit (Mihalas & Mihalas 1984), when the dynamical timescale of a fluid flow is shorter than the radiation-ion equilibrium timescale. This tends to be true in regions of high optical depth and some accretion streams, but can fail in the boundary layer between optically thick and thin regions (Boley et al. 2006; Kuiper et al. 2010; Ohsuga et al. 2005).

However, the optical depth transition region is important to our work, so we cannot use a simple, one temperature approach. We also cannot evolve the hydrodynamics on the short timesteps implied in high opacity regions of our simulations. Therefore, we are forced to adopt a new radiation-matter coupling solver, described below.

2.4. Exact Integration of the Radiation-Matter Coupling

In Section 2.3, we identified several issues that arise with the standard FLASH radiation-matter coupling algorithm when it is applied to astrophysical problems. Here, we describe our modifications to the solver to overcome these problems.

The FLASH code supports energy transfer between the ions and electrons via the thermal conductivity module. This module was primarily intended for use in high-energy density physics (e.g. laboratory laser) experiments. Currently, Spitzer heat conductivity (Atzeni et al. 2004) is the only method in the distribution version of FLASH to transfer energy from the electrons to the ions in a gas. In astrophysical situations, the timescale for thermal equilibrium is typically much shorter than other relevant dynamical timescales, and therefore tends to be many orders of magnitude shorter than the hydrodynamic timesteps in simulation. Therefore, we assume that the ions and electrons quickly reach equilibrium every timestep, and the timescale of this process is of no consequence. This equilibrium temperature can be found via

$$u_{\text{ele}} + u_{\text{ion}} = \frac{\rho R T_{\text{eq},2T}}{\bar{A}(\gamma-1)} + \frac{Z \rho R T_{\text{eq},2T}}{\bar{A}(\gamma-1)}, \quad (14)$$

where R is the gas constant, $T_{\text{eq},2T}$ is the electron-ion equilibrium temperature, $\gamma = 5.0/3.0$ for the matter, as described in Section 2.5, and \bar{A} is the mean molecular mass. For this work, we assume $Z = \bar{A} = 1$ for our pure hydrogen gas, fully-ionized, which means $u_{\text{ele}} = u_{\text{ion}}$ at all times in our simulation. This makes our simulation, effectively, a two temperature (2T) code, as we only are concerned with the matter temperature, $T_{\text{ele}} = T_{\text{ion}}$, and the radiation temperature T_{rad} .

In order to avoid the prohibitive timestep constraint introduced in Equation 12, we choose to numerically integrate the equation for radiation-electron coupling. We start with the single-group equation radiation-electron coupling

$$\frac{\partial u_{\text{ele}}}{\partial t} = c (\sigma_a u_{\text{rad}} - \sigma_e a T_{\text{ele}}^4). \quad (15)$$

Although not necessary for this method, here we will make the astrophysically relevant assumption that $\sigma_a = \sigma_e = \sigma$. Note that σ does not take the transport opacity into account.

We further restrict our problem by assuming that σ is held constant; it does not vary greatly with temperature during the energy-matter coupling process. This is not entirely accurate in all regimes, but as long as the form of our opacity is relatively smooth, it may not be a large issue. Because we assume that ions and electrons instantaneously enter temperature equilibrium, we must rewrite our equation to account for the transfer of energy from the radiation field to both ions and electrons. We can then rewrite Equation 15 in terms of u_{tot}

$$\begin{aligned} \frac{\partial u_{\text{ele}}}{\partial t} &= c\sigma (u_{\text{tot}} - 2u_{\text{ele}} - aT_{\text{ele}}^4) \\ \frac{\partial u_{\text{ele}}}{\partial t} &= c\sigma \left(u_{\text{tot}} - 2u_{\text{ele}} - a \left[\frac{\bar{A}(\gamma-1)}{\rho R} \right]^4 u_{\text{ele}}^4 \right) \end{aligned} \quad (16)$$

The exact value of u_{ele} for the next time step can be found using a polynomial root finder or quartic solver. We must then integrate

$$\int_{t_0}^t \partial t = \int_{u_{\text{ele}}(t_0)}^{u_{\text{ele}}(t)} \frac{\partial u_{\text{ele}}}{c\sigma \left(u_{\text{tot}} - 2u_{\text{ele}} - a \left[\frac{\bar{A}(\gamma-1)}{\rho R} \right]^4 u_{\text{ele}}^4 \right)}, \quad (17)$$

where t_0 is the time at the start of the timestep, and $t = t_0 + \Delta t$ is the time at the end of the radiative timestep. A simple analytic solution to Equation 16 does not exist, and must be numerically integrated. We have utilized the C GSL quags integrator to carry out this calculation in our code. The value of $u_{\text{ele}}(t)$ is unknown and is ultimately the value we desire, so a bisection solver is then used to iterate over values of $u_{\text{ele}}(t)$ until the desired value of t is returned by the solver. We find that in most situations, the entire radiation solver accounts for < 10% of the total runtime of the simulation.

After each timestep, the solver returns the value of $u_{\text{ele}}(t)$, and the value of $u_{\text{rad}}(t)$ is recovered via $u_{\text{rad}}(t) = u_{\text{tot}} - 2.0u_{\text{ele}}$. In situations where $u_{\text{ele}} = u_{\text{ion}} \gg u_{\text{rad}}$, numerical error in the value returned for u_{ele} may overwhelm the value of u_{rad} . In this case, we must instead rewrite the corresponding equation for Equation 16 in terms of u_{rad}

$$\frac{\partial u_{\text{rad}}}{\partial t} = 2c\sigma \left(a \left[\frac{\bar{A}(\gamma-1)}{\rho R} \right]^4 \left[\frac{u_{\text{tot}} - u_{\text{rad}}}{2} \right]^4 - u_{\text{rad}} \right), \quad (18)$$

which can then be integrated in a similar fashion to Equation 17

$$\int_{t_0}^t \partial t = \int_{u_{\text{rad}}(t_0)}^{u_{\text{rad}}(t)} \frac{\partial u_{\text{rad}}}{c\sigma \left(a \left[\frac{\bar{A}(\gamma-1)}{\rho R} \right]^4 \left[\frac{u_{\text{tot}} - u_{\text{rad}}}{2} \right]^4 - u_{\text{rad}} \right)}. \quad (19)$$

The solution of this will be converged upon again using the method above. In either method, care is taken to ensure that in cases where the gas is already at or very near equilibrium at the start of a timestep, no expensive computations are performed.

This method guarantees that, if the above assumptions are true, $T_{\text{ele}} = T_{\text{ion}}$ at all times, as long as this was true during the initialization of the simulation. Since we have integrated the coupling exactly, there is no inherent timestep constraint for this method. It is important to note, however, that this coupling is completely operator split from radiative diffusion. Both diffusion and radiation-matter coupling should be numerically stable as long as the above criteria are met. Conservation errors may grow in highly diffusive situations where a

large computational timestep is taken relative to the diffusive timescale. A timestep limiter of the form

$$\Delta t_{\text{max,FLD}} = \alpha_{\text{FLD}} \frac{u_{\text{FLD}}}{\Delta u_{\text{FLD}}}, \quad (20)$$

where $\alpha_{\text{FLD}} \ll 1$ is a constant value, chosen for stability. This ensures that dramatic changes in the temperature of the gas cannot occur over a single timestep to prevent numerical instability brought about by gas pressure coupling with the hydrodynamics.

2.5. Equation of State

We treat our gas as a fully ionized pure hydrogen gas. We utilize a multispecies γ -law equation of state, where the $\gamma = 5.0/3.0$ for ions and electrons and $\gamma = 4.0/3.0$ for radiation. In our modification of the FLASH code, we ensure that at all times, $T_{\text{ion}} = T_{\text{ele}}$, but treat T_{rad} independently.

This is certainly an oversimplification, especially in the conditions of cool molecular clouds around protostars or in potentially hot atmospheres in the winds of massive stars where electrons may become relativistic. However, the focus of this work is to investigate the general structure and behavior of instabilities that may form in SE atmospheres, not to replicate the exact details of any specific atmosphere.

The specific entropy of an ideal, fully ionized, pure H gas is

$$\begin{aligned} s &= s_e + s_p + s_r \\ &= \frac{k}{\rho} n_e \left\{ \frac{5}{2} + \ln \left[\frac{2}{n_e} \left(\frac{m_e k T}{2\pi \hbar^2} \right)^{3/2} \right] \right\} \\ &\quad + \frac{k}{\rho} n_p \left\{ \frac{5}{2} + \ln \left[\frac{2}{n_p} \left(\frac{m_p k T}{2\pi \hbar^2} \right)^{3/2} \right] \right\} + \frac{4}{3} \frac{a T^3}{\rho} \end{aligned} \quad (21)$$

2.6. Opacity

We implement the Kramer free-free opacity for a pure H gas

$$\kappa(\rho, T \geq 10^4 \text{ K}) = 3.68 \times 10^{22} \rho \left(\frac{T}{\text{K}} \right)^{-7/2} \quad (22)$$

in regions where $T \geq 10^4$ K. When the temperature falls below this threshold, we implement a simple functional form $\kappa \propto T^6$ to approximate the steep decline seen in opacity as the ionization state decreases. We ensure the function of the opacity is continuous by giving it the following form for $T < 10^4$ K

$$\kappa(\rho, T < 10^4 \text{ K}) = \rho \left(\frac{T}{k} \right)^6 - \rho \left(\frac{10^4}{k} \right)^6 + \kappa(\rho, 10^4 \text{ K}). \quad (23)$$

The above opacities are used in the calculation of $\sigma_a = \sigma_e = \kappa \rho$.

We include the effects of electron scattering

$$\kappa_{\text{es}} = 0.2 \quad (24)$$

This is added to the transport opacity, $\sigma_t = \kappa + \kappa_{\text{es}}$.

$$(25)$$

3. ASSESSMENT AND TESTS OF THE CODE

3.1. Diffusion of a Gaussian Pulse

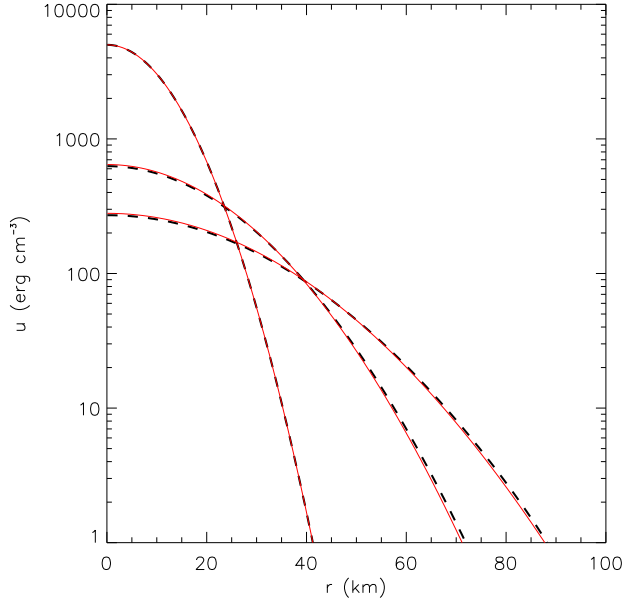


FIG. 1.— The diffusion of a Gaussian pulse problem posed by (Swesty & Myra 2009; Sumiyoshi & Yamada 2012) with initial conditions from Abdikamalov et al. (2012). The red, solid lines represent the exact, analytical solution, and the black, dashed lines represent the results of our simulation at times $t = 0, 30$ ms, and 60 ms, in descending order of peak energy. We show a high level agreement with the analytic results, as is to be expected with an FLD code.

In order to test the codes ability to handle radiation diffusion properly, we consider a Gaussian pulse of radiation diffusion into a medium with only scattering opacity ($\sigma_a = \sigma_e = 0$). This problem can be solved analytically (Swesty & Myra 2009; Sumiyoshi & Yamada 2012). The diffusion of a Gaussian packet with initial central position at $r = r_0$ and width d_0 in one dimension is described by

$$E(r, t) = E_0 \left(\frac{t_0}{t_0 + t} \right)^{0.5} \exp \left(\frac{-|r - r_0|^2}{4D(t_0 + t)} \right), \quad (26)$$

where $E(r, t)$ is the radiation energy density at position r and time t with initial time t_0 , E_0 is the initial peak radiation energy density, and $D = \frac{c}{3\sigma_t}$.

We replicate the initial conditions of Abdikamalov et al. (2012), who also used this test problem. The Gaussian pulse was centered around the center of our computational domain and the maximum radius of our simulation was set to 300 km, $d_0 = 10$ km, $E_0 = 5.0 \times 10^3$ erg cm $^{-3}$, and $\sigma_t = 2 \times 10^{-4}$ cm $^{-1}$. We initialize the pulse via

$$u_r = E_0 \exp \left(-\frac{r^2}{2d^2} \right). \quad (27)$$

The results are shown in Figure 1. We find a high level of agreement with the analytic results, and have confirmed that this holds in a variety of other parameter ranges.

3.2. Heated Exponential Atmosphere

Here we consider an atmosphere with initial uniform temperature T_0 , constant opacities σ_a , σ_e , and σ_t , and a mass density profile given by

$$\rho = \rho_0 e^{-\frac{x}{x_0}} \quad (28)$$

in one dimension in Cartesian coordinates. The electrons in the gas are uniformly heated at the constant rate ϵ in units of

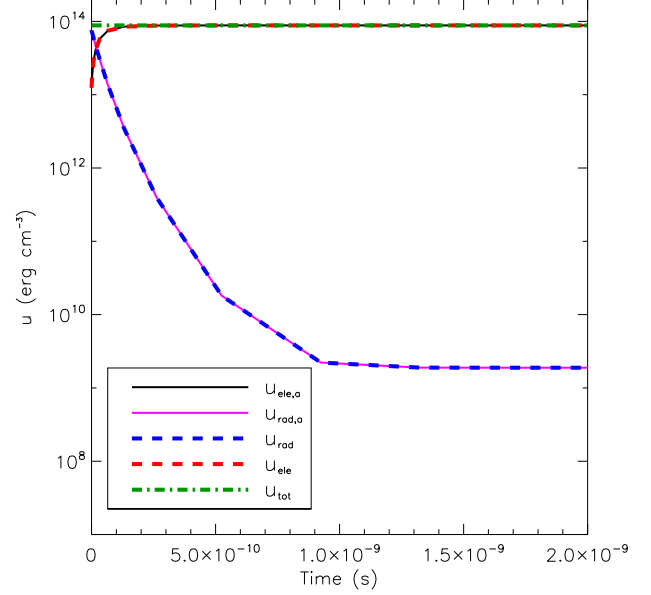


FIG. 2.— A simple test of our matter-radiation coupling solver as described in Section 3.3. In this test, the initial conditions are $T_{\text{rad}} = 10^7$ K, $T_{\text{ele}} = 10^5$ K, $\sigma_a = \sigma_e = 1.0$ cm $^{-1}$. The black and pink solid lines represent the previous solver's discretized solutions for the evolution of u_{ele} and u_{rad} , respectively. The bold blue dashed line and bold red dashed line represent the values of u_{ele} and u_{rad} returned by our new solver. The green dash-dotted line shows the (constant) total energy, u_{tot} . We find a high level of agreement between our solver and the previous.

erg s $^{-1}$ g $^{-1}$. The hydrodynamic evolution of the gas is ignored in this problem ($v = 0$). The inner ($x = x_{\text{min}}$) radiation boundary is set to reflect radiation, while the outer boundary ($x = x_{\text{max}}$) is treated as a vacuum.

The goal of this test is to evaluate gas heating and cooling and transfer of radiation in an atmosphere that is optically thick near x_{min} and optically thin near x_{max} .

In a steady state, the total energy input over the entire box must be radiated at the outer boundary,

$$\int_{x_{\text{min}}}^{x_{\text{max}}} \rho(x) \epsilon dx = F_{\text{rad}}(x_{\text{max}}). \quad (29)$$

3.3. Single-Zone Heating and Cooling

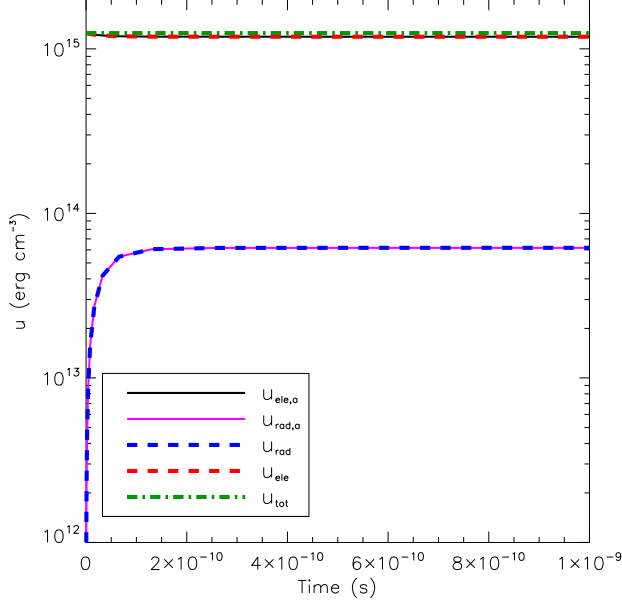
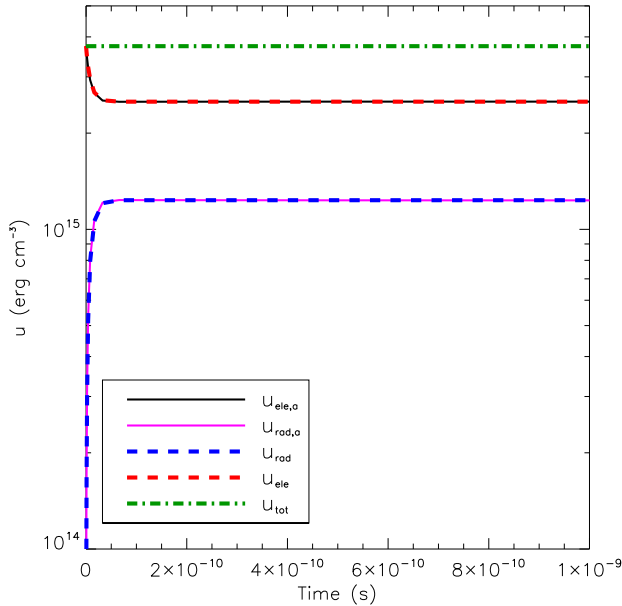
For this test we consider a single-zone fluid where at the start of the simulation the radiation is out of equilibrium with the fluid. The free parameters are the static, constant density $\rho_0 = 1.0$ g cm $^{-3}$, the initial radiation temperature $T_{\text{rad},0}$, the initial gas temperature $T_{\text{gas},0}$, and the emission and absorption coefficients σ_e and σ_a in units of cm $^{-1}$.

In this situation, the derivative of the energy density of the electrons with time is

$$\partial_t u_{\text{ele}} = c \sum_g \left\{ \sigma_a u_{r,g} - \sigma_e a T_e^4 \frac{15}{\pi^4} [P(x_{g+1}) - P(x_g)] \right\} \quad (30)$$

where the summation is performed over the radiation bands in MGD, c is the speed of light, $u_{r,g}$ is the radiation energy density for a given band, a is the radiation constant, T_e is the electron temperature, P is the Planck function, and x is the Planck argument. In the presence of a single band $g = 1$ of radiation which effectively covers the frequency range $0 < \nu < \infty$, $P(x_0) = 0$ and $P(x_1) = \pi^4/15$. Equation 30 simplifies to

$$\partial_t u_{\text{ele}} = c (\sigma_a u_{\text{rad}} - \sigma_e a T_e^4). \quad (31)$$

FIG. 3.— As Figure 2, except $T_{\text{rad}} = 10^5$ K, $T_{\text{ele}} = 10^7$ K.FIG. 4.— As Figure 2, except $T_{\text{rad}} = 10^3$ K, $T_{\text{ele}} = 3 \times 10^7$ K.

Discretizing and ignoring diffusive terms, the standard FLASH radiation-matter coupling solver solves the following equation for the radiation energy density first

$$\frac{1}{c} \frac{u_r^{n+1} - u_r^n}{\Delta t} + \sigma_a u_r^{n+1} = \sigma_e a (T_e^n)^4, \quad (32)$$

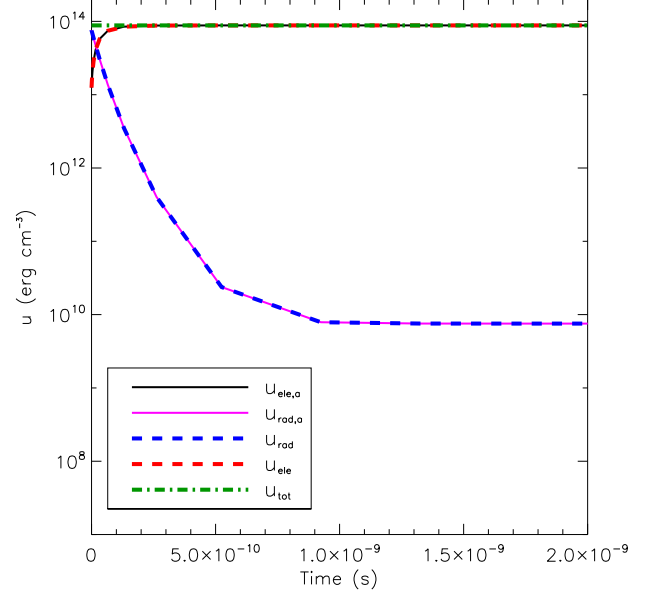
where n is the current step. This can be rewritten as

$$u_r^{n+1} = \frac{u_r^n + c \Delta t \sigma_e a (T_e^n)^4}{1 + \sigma_a c \Delta t}. \quad (33)$$

Then the electron energy density is calculated via

$$u_e^{n+1} = u_e^n + c \Delta t [\sigma_a u_r^{n+1} - \sigma_e a (T_e^n)^4]. \quad (34)$$

Our modified solver is described in Section 2.4. In this test

FIG. 5.— As Figure 2, except $\sigma_e = 4.0$

we compare the results of our solver to that of FLASH. The initial conditions and results of these tests are shown in Figures 2, 3, 4, and 5. We find strong agreement between the two solvers. Our solver, however, has the advantage of avoiding the timestep restrictions mentioned in Section 2.3.

3.4. Heated Hydrostatic Atmosphere

Here we recreate the heated slab radiation test problem presented in Hubeny (1990) and Boley et al. (2007), which includes an exact, analytic solution. We initialize an isothermal, isodensity atmosphere with a constant gravitational acceleration g in the $-x$ direction. The $-x$, $+y$, and $-y$ boundaries are reflecting, and the $+x$ boundary is set to outflow. The atmosphere is heated at a constant rate defined as

$$\Gamma = \pi F_0 \frac{\sigma}{\tau_m}, \quad (35)$$

where $F_0 = \sigma_{\text{SB}} T_{\text{eff}}^4 / \pi$ is the effective astrophysical flux from an atmosphere with effective temperature T_{eff} , τ_m is the optical depth at the midplane. Gravity accelerates the atmosphere and causes it to stratify and cool until it reaches a configuration where the flux from the surface is able to carry away the heat generated from our artificial heating. The exact analytic temperature solution for a steady state atmosphere in this configuration is

$$T^4 = \frac{3}{4} T_{\text{eff}}^4 \left[\tau \left(1 - \frac{\tau}{2\tau_m} \right) + \frac{1}{\sqrt{3}} \right]. \quad (36)$$

We recreate the initial conditions from Boley et al. (2007) and find a profile similar to that predicted in Equation 36.

4. SIMULATION PARAMETERS

These simulations are carried out in two spatial dimensions, (x, z) . Three dimensional effects may be important when considering convective and other instabilities, and we leave this for future work. Our simulations have a constant gravitational acceleration g in the $-x$ direction. The $+y$, $-x$, and $-y$ boundary conditions are set to reflecting both hydrodynamically and radiatively. The $+x$ boundary is set to be outflow hydrodynamically, and set to simulate a vacuum radiatively.

We initialize our atmospheres to be in isothermal hydrostatic equilibrium, neglecting any radiative heating or cooling; if left for sufficient time without any heating, these atmospheres would cool and shrink. However, the cooling times of these atmospheres are longer than our simulation durations, and the heating rate in our heated atmospheres will typically be greatly exceed the much slower cooling timescale.

Heat is inject at zones $x < x_{\text{heat}}$ at a rate $\dot{\epsilon}_{\text{heat}}$. Energy is only added to the radiation field.

4.1. Vacuum Boundary Conditions

Vacuum boundary conditions apply

$$\chi = \frac{AB}{2} \frac{\Delta t}{\Delta x} \left[1 - \frac{2B/(c\Delta x) - 0.5}{2B/(c\Delta x) + 0.5} \right], \quad (37)$$

where A is the area of the face of a cell and

$$B = \frac{c}{3\sigma_1}. \quad (38)$$

5. SIMULATION RESULTS

Several simulations of toy atmospheres have been performed so far, with a variety of predicted phenomena occurring. In Figures 6 and 7, we see radiation forming low-optical depth channels in the atmosphere, giving radiation a easier path of escape. In Figure 8, we see the evidence for the radiative Rayleigh-Taylor instability, ultimately helping to seed convection in a very optically thick atmosphere. In Figure 9, we see a SE atmosphere launching low density winds, and breaking dense, wispy clumps from its surface.

6. DISCUSSION

7. CONCLUSIONS

The software used in this work was in part developed by the DOE-supported ASC/Alliance Center for Astrophysical Thermonuclear Flashes at the University of Chicago. The authors acknowledge the Texas Advanced Computing Center (TACC) at the University of Texas at Austin for providing high-performance computing resources that have contributed to this research. C. C. L. acknowledges support from a National Science Foundation Graduate Research Fellowship. M. M. acknowledges support from NSF grants AST-0708795 and AST-1009928.

REFERENCES

- Abdikamalov, E., Burrows, A., Ott, C. D., et al. 2012, arXiv:1203.2915
- Atzeni, S., Schiavi, A., & Temporal, M. 2004, *Plasma Physics and Controlled Fusion*, 46, 111
- Blaes, O., & Socrates, A. 2003, *ApJ*, 596, 509
- Boley, A. C., Mejia, A. C., Durisen, R. H., et al. 2006, *ApJ*, 651, 517
- Boley, A. C., Hartquist, T. W., Durisen, R. H., & Michael, S. 2007, *ApJ*, 656, L89
- Dotan, C., & Shaviv, N. J. 2012, *MNRAS*, 427, 3071
- Fan, X., Narayanan, V. K., Lupton, R. H., et al. 2001, *AJ*, 122, 2833
- Fan, X., Strauss, M. A., Schneider, D. P., et al. 2003, *AJ*, 125, 1649
- Fryxell, B., Olson, K., Ricker, P., et al. 2000, *ApJS*, 131, 273
- Gittings, M., Weaver, R., Clover, M., et al. 2008, *Computational Science and Discovery*, 1, 015005
- Hubeny, I. 1990, *ApJ*, 351, 632
- Jacquet, E., & Krumholz, M. R. 2011, *ApJ*, 730, 116
- Krumholz, M. R., Klein, R. I., McKee, C. F., Offner, S. S. R., & Cunningham, A. J. 2009, *Science*, 323, 754
- Krumholz, M. R., & Thompson, T. A. 2012, *ApJ*, 760, 155
- Krumholz, M. R., & Thompson, T. A. 2013, *MNRAS*, 434, 2329
- Kuiper, R., Klahr, H., Dullemond, C., Kley, W., & Henning, T. 2010, *A&A*, 511, A81
- Kuiper, R., & Yorke, H. W. 2012, arXiv:1211.6432
- Lindner, C. C., Milosavljević, M., Couch, S. M., & Kumar, P. 2010, *ApJ*, 713, 800
- Lindner, C. C., Milosavljević, M., Shen, R., & Kumar, P. 2012, *ApJ*, 750, 163
- Mihalas, D., & Mihalas, B. W. 1984, New York, Oxford University Press, 1984, 731 p.,
- Morel, J. E., & McClarren, R. 2011, *J. Quant. Spec. Radiat. Transf.*, 112, 1518
- Mortlock, D. J., Warren, S. J., Venemans, B. P., et al. 2011, *Nature*, 474, 616
- Ohsuga, K., Mori, M., Nakamoto, T., & Mineshige, S. 2005, *ApJ*, 628, 368
- Ohsuga, K., & Mineshige, S., Mori, M., & Kato, Y. 2009, *PASJ*, 61, L7
- Ohsuga, K., & Mineshige, S. 2011, *ApJ*, 736, 2
- Shaviv, N. J. 2000, *ApJ*, 532, L137
- Shaviv, N. J. 2001, *ApJ*, 549, 1093
- Shaviv, N. J. 2001, *MNRAS*, 326, 126
- Spiegel, E. A., & Tao, L. 1999, *Phys. Rep.*, 311, 163
- Sumiyoshi, K., & Yamada, S. 2012, *ApJS*, 199, 17
- Swesty, F. D., & Myra, E. S. 2009, *ApJS*, 181, 1
- Turner, N. J., & Stone, J. M. 2001, *ApJS*, 135, 95
- van Marle, A. J., Owocki, S. P., & Shaviv, N. J. 2008, *MNRAS*, 389, 1353
- van Marle, A. J., Owocki, S. P., & Shaviv, N. J. 2009, *MNRAS*, 394, 595

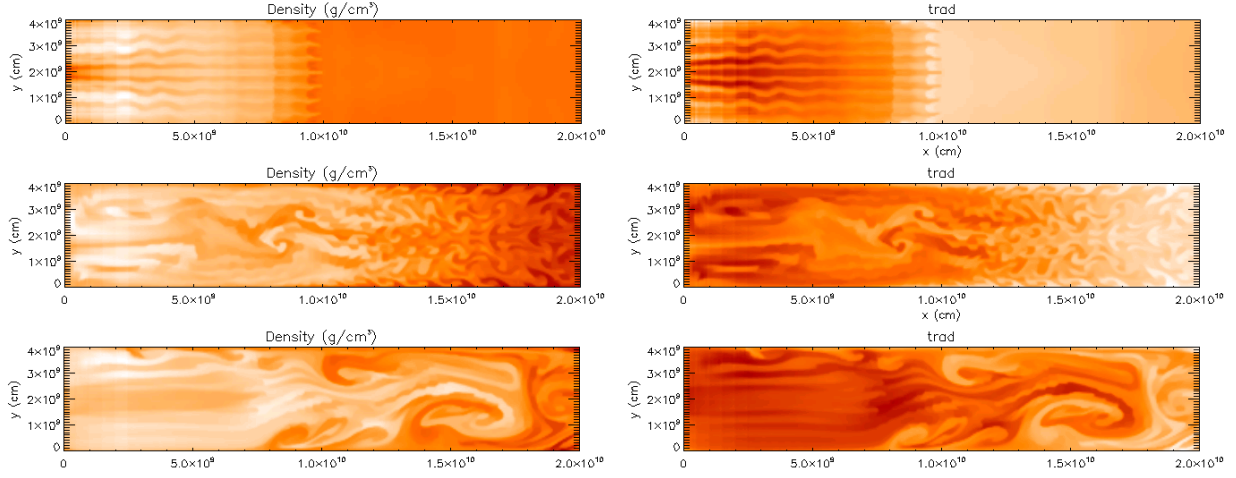


FIG. 6.— The densities (left) and radiation temperatures (right) of a atmosphere heated at the base at a SE rate. In the initial model, $\rho_{\text{base}} \sim 1 \text{ g cm}^{-3}$, $g = 10^3 \text{ cm s}^{-2}$, $\epsilon = 10^{13} \text{ erg g}^{-1}$. From top to bottom, the times of each snapshot are 1000, 5000, and 10000 s. The mach number of the flow in the hottest regions ~ 0.1 . Note the "fingers" bored in the flow at early times. These channels have the lowest densities and the highest radiation temperatures, and radiation is able to leave through these channels without encountering the higher density regions. The optical depth of the channels is $\approx 10\%$ that of the denser regions. The propagation of the radiation is slowed by the higher density regions at the head of the outflow. The flow is subject to further instabilities as it accelerates.

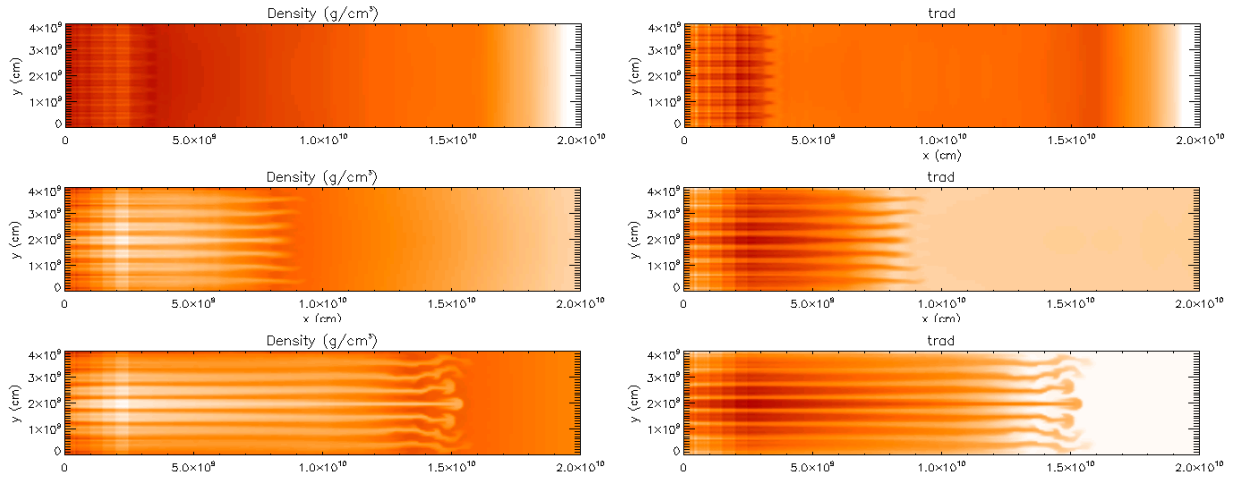


FIG. 7.— As Figure 6, but with 0 of the heating rate. Here, hot, radiation dominated channels again form, but the gas moves at about half the velocity. The large scale instabilities have not yet formed here.

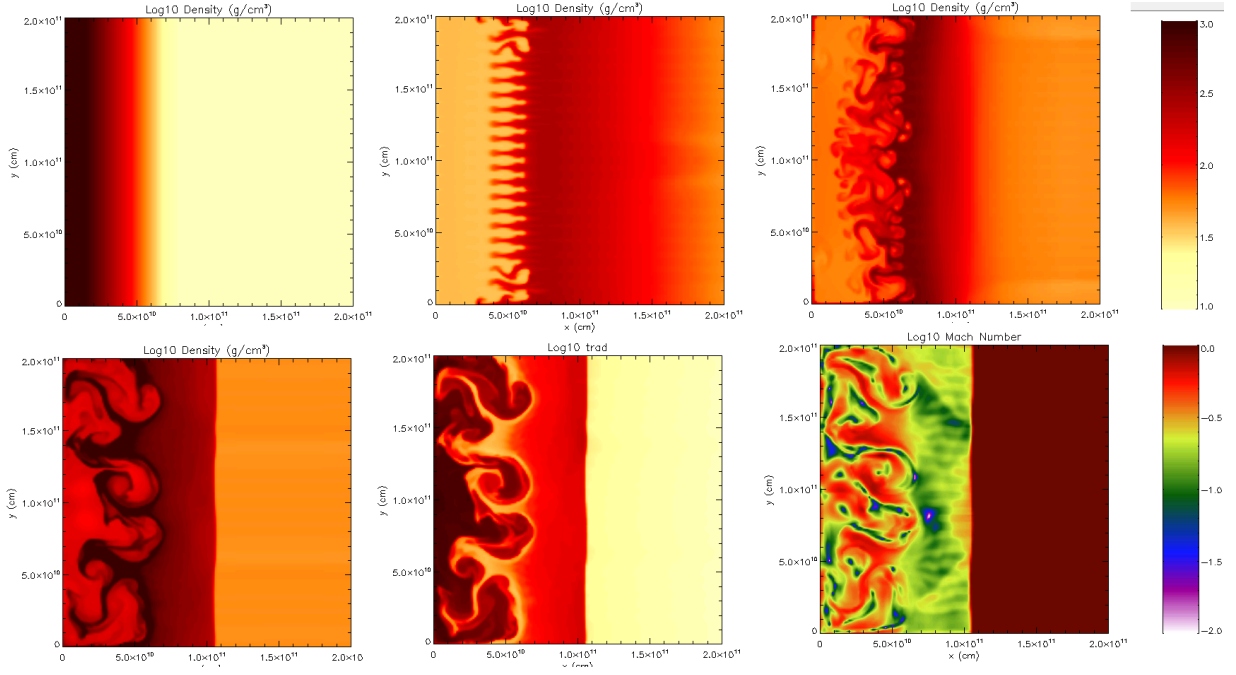


FIG. 8.— Here, a higher density, lower-heating rate atmosphere demonstrates the radiative Rayleigh-Taylor instability. The density panels show times $t = 0, 5000, 10000, 15000$ s, with the last time being in the lower left hand corner. As energy is injected initially, it cannot be efficiently radiated, and the lower layers of the atmosphere begin to swell and drop in density. This density inversion drives a Rayleigh-Taylor instability, as fingers begin to form on the low-density, high-density boundary located at $x \sim 5 \times 10^{10}$ cm in the second panel. In the third panel (top right corner), we see that the RT instability has helped seed convective motions, and by the fourth panel, we see convection is efficiently transporting energy from the base of the atmosphere. The temperature panel at $t = 15000$ s shows that radiation has difficulty escaping the dense, very optically thick convective region. The final panel shows the mach number of the fluid; convective motions approach the sound speed of the fluid. No outflow is driven in this simulation.

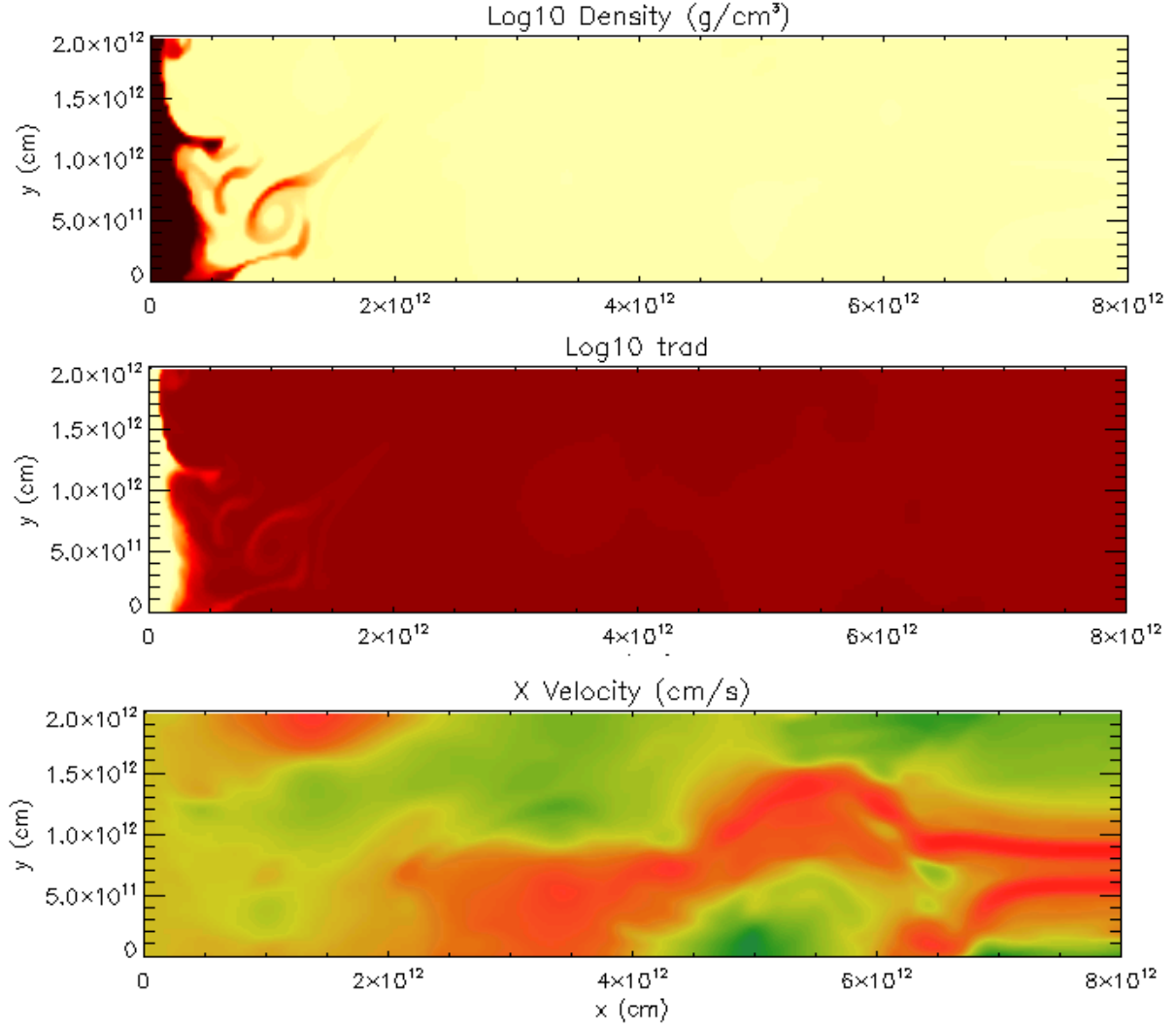


FIG. 9.— A dense atmosphere driving a wind from its surface. We see wispy, dense material being flung off the surface of the atmosphere, but radiation cannot penetrate it. Instead, it will fall back down and radiation will escape through the lower density, lower opacity regions around it. In the bottom panel, green and yellow colors indicate a positive x velocity, while red colors indicate a negative velocity. We see some low density material has formed a thin channel to escape from.